



Cite this: DOI: 10.1039/d6sc02671k

All publication charges for this article have been paid for by the Royal Society of Chemistry

## Decoding cryptic defluorinases through a latent generative sequence landscape

Ke Ji,<sup>†a</sup> Sydney S. Barnes,<sup>†a</sup> Cheyenne Ziegler,<sup>†b</sup> Marjan Nikpey,<sup>c</sup> Jose Alberto de la Paz,<sup>†d</sup> Elizabeth K. Pack,<sup>a</sup> Nikita Kvasovs,<sup>†e</sup> Faruck Morcos<sup>†\*bcde</sup> and Sheel C. Dodani<sup>†\*a</sup>

The special nature of the fluorine atom imparts remarkable strength and unique physical properties to chemical bonds. Unlike man-made fluorochemicals, fluorinated natural products remain rare due to low bioavailability and toxicity of fluoride. Despite this, defluorinases have evolved in nature to cleave carbon-fluorine bonds, with the hydrolytic fluoroacetate dehalogenase being one of the most well-characterized examples. These enzymes are of fundamental interest and hold unrealized biotechnological potential, yet the scope of this unique chemistry remains underexplored in the biosphere. Here, we trained and applied a machine learning-based framework, termed latent generative landscapes (LGLs), to map the functional sequence space of the  $\alpha/\beta$ -hydrolase superfamily. This approach identified 3014 putative defluorinases that were previously not annotated or plausibly misannotated. Experimental validation of selected candidates led to the reclassification of five novel defluorinases, all exhibiting high thermal stability ( $T_m > 70$  °C) and diverse catalytic efficiencies with conserved enantioselectivity on the model substrate 2-fluoro-2-phenylacetate. Notably, the enzyme A0A4Z0BVY8 exhibited 2.7-fold greater defluorination activity than the current state-of-the-art enzyme Q6NAM1. Our results establish that LGL modeling is a powerful strategy to decode cryptic carbon–fluorine bond chemistry in nature, enabling the future discovery and engineering of defluorination biocatalysts.

Received 31st March 2026  
Accepted 23rd May 2026

DOI: 10.1039/d6sc02671k

rsc.li/chemical-science

## Introduction

Of the halogens, fluorine is the most abundant in the Earth's crust.<sup>1–3</sup> However, it is largely hidden from the biological world, sequestered in minerals in the form of fluoride.<sup>2,4</sup> Only in rare cases is fluorine incorporated into natural products, with fluoroacetate being the simplest known example.<sup>4–6</sup> While carbon–fluorine bond formation is mediated by a single enzyme class, naturally occurring enzymes that can cleave carbon–fluorine bonds have evolved across multiple classes, accessing a wider range of mechanistic solutions, in some cases through promiscuous activity.<sup>7–30</sup> Among these, hydrolytic defluorination mediated by fluoroacetate dehalogenases from the  $\alpha/\beta$ -hydrolase superfamily (ABH; Pfam: PF00561) represents a well-characterized strategy.<sup>31–33</sup> Efforts have primarily focused on

understanding these enzymes through computational modeling, mechanistic enzymology, and structural biology, with the fluoroacetate dehalogenase from *Rhodopseudomonas palustris* (UniProt Accession Number: Q6NAM1) serving as the most extensively studied member (Fig. 1A).<sup>14,34–40</sup>

In Q6NAM1, the entry of fluoroacetate is gated by W185, and recognition in the active site relies on carboxylate anchoring residues R111 and R114 (Fig. 1B).<sup>14</sup> The defluorination mechanism proceeds *via* an  $S_N2$  mechanism, in which a nucleophilic attack by D110 displaces fluoride to form a transient covalent intermediate, followed by hydrolysis mediated by D134 and H280 to release hydroxyacetate and a proton (Fig. 1C).<sup>14,35,37–39,41</sup> Fluoride stabilization is facilitated by H155, W156, and Y219, and mutations at these positions can not only tune catalytic efficiency but also shift halide selectivity.<sup>14,42,43</sup> Q6NAM1 can also transform  $\alpha$ -fluoro-carboxylic acids such as 2-fluoro-2-phenylacetate with stereochemical preference (Fig. 1C).<sup>37,43</sup> More recently, Q6NAM1 and other fluoroacetate dehalogenases have attracted attention as biocatalysts for kinetic resolution of  $\alpha$ -fluoro-carboxylic acids and degradation of anthropogenic organofluorine compounds, underscoring their biotechnological potential.<sup>22,25,44,45</sup> At the same time, microbial genome mining and homology-based annotation suggest that hydrolytic defluorination may be more widespread than currently recognized.<sup>23,46–50</sup>

<sup>a</sup>Department of Chemistry and Biochemistry, The University of Texas at Dallas, Richardson, TX 75080, USA. E-mail: sheel.dodani@utdallas.edu

<sup>b</sup>Department of Biological Sciences, The University of Texas at Dallas, Richardson, TX 75080, USA. E-mail: faruckm@utdallas.edu

<sup>c</sup>Department of Bioengineering, The University of Texas at Dallas, Richardson, TX 75080, USA

<sup>d</sup>Department of Physics, The University of Texas at Dallas, Richardson, TX 75080, USA

<sup>e</sup>Center for Systems Biology, The University of Texas at Dallas, Richardson, TX 75080, USA

<sup>†</sup> These authors contributed equally to this work.



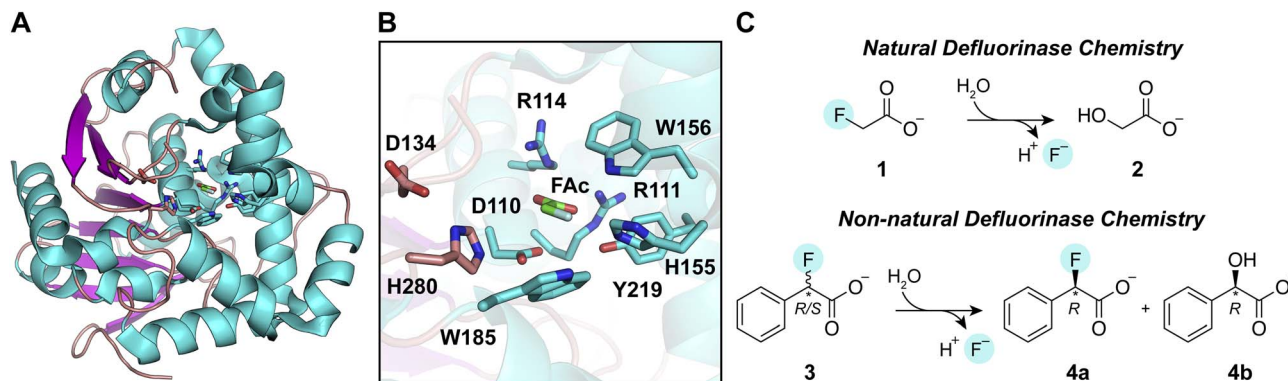


**Fig. 1** (A) Crystal structure of the fluoroacetate dehalogenase from *Rhodospseudomonas palustris* (UniProt Accession Number: Q6NAM1; PDB ID: 3R3V). For this representation, N110 was reverted to D110 in PyMOL. (B) The enzyme active site with fluoroacetate (FAc) bound. Select residues within 4 Å of FAc are shown. (C) Q6NAM1 can defluorinate (top) the natural product fluoroacetate (compound 1) into hydroxyacetate (compound 2) and (bottom) the non-natural substrate racemic 2-fluoro-2-phenylacetate (compound 3) into (R)-2-fluoro-2-phenylacetate (compound 4a) and (R)-2-hydroxy-2-phenylacetate (compound 4b).

Despite this growing interest, functional assignment across the ABH superfamily remains challenging because of the large number of members (977 130; Swiss-Prot and TrEMBL, release prior to 2024) that share a high degree of sequence and structural similarity yet span diverse and even promiscuous chemistries.<sup>51,52</sup> As a result, scalable and accurate annotation methods are needed to systematically map sequence space to defluorination activity. Recent advances in computational and machine learning approaches provide new opportunities to address this gap by integrating large-scale sequence information with experimental datasets to build predictive models.<sup>53–57</sup>

Latent generative landscapes (LGLs) provide one such approach as they are maps created from protein sequence data that illustrate how sequence diversity connects to function.<sup>58</sup> By integrating Variational Autoencoders (VAE) alongside Direct Coupling Analysis (DCA), LGLs learn not only which individual residues are key for functional and phylogeny classification but also how important interactions between residues are indicative of features within the family that define functional and fitness relationships.<sup>58–62</sup> This helps researchers investigate protein diversity, predict functional integrity, and create new variants while maintaining the networks crucial for protein activity. LGLs have been used to study thermal adaptation in cytosolic malate dehydrogenases, and its generative properties have produced viable functional sequences encoding multidomain ATPase metal transporters.<sup>63,64</sup> By capturing higher-order relationships in sequence space beyond simple sequence identity, this approach could distinguish among the closely related, structurally similar ABH sequences while providing an interpretable framework to explore and guide hypotheses and experimental inquiries. Here, we trained and applied the LGL framework to classify carbon–halogen bond chemistries and uncover novel defluorinases with experimental validation from the visualized sequence space of the ABH superfamily.

## Experimental

### General

All reagents and supplies used in this study were acquired from AmBeed, Research Products International, Sigma-Aldrich, Thermo Fisher Scientific, USA Scientific, and VWR International, with exceptions noted.

### Multiple sequence alignment (MSA) generation for training the LGL

An overview of the workflow for the training and application of the LGL is shown in Fig. S1. The  $\alpha/\beta$ -hydrolase (ABH) MSA was obtained by running a *hmmsearch* (<https://hmmer.org>) against the UniProt Knowledgebase (Swiss-Prot and TrEMBL, release prior to 2024), with the corresponding Pfam Hidden Markov Model (HMM) profile (Pfam ID: PF00561, Accessed 2023) using the Ganymede 2 High Performance Computing at UT Dallas, resulting in 977 130 sequences.<sup>40,51,65</sup> Sequences were aligned with HMMER and aligned sequences with more than 20 contiguous gaps were excluded. The training MSA consisted of the subset of sequences annotated in Gene Ontology (GO:0016824) as hydrolases acting on acid-halide bonds (2753 sequences) using the QuickGO API (Fig. S2).<sup>66,67</sup>

### Latent generative landscape

LGLs provide a framework for analyzing the organization of protein sequence space by combining deep generative modeling with coevolutionary analysis.<sup>58</sup> In this approach, a variational autoencoder (VAE) is trained on an MSA to learn a two-dimensional latent representation that captures the statistical structure of a protein family. The latent space is then systematically sampled, and sequences generated from each latent coordinate are evaluated using a direct coupling analysis (DCA) derived Potts Hamiltonian score, which reflects evolutionary constraints between amino acid positions.<sup>59</sup> Mapping these scores across the latent coordinates produces a latent generative landscape in which low Hamiltonian scores



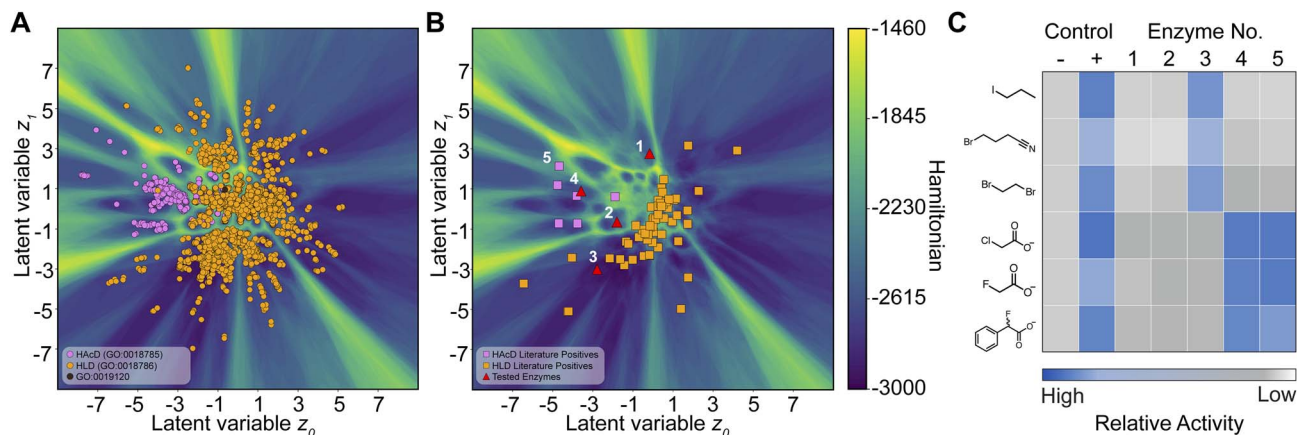


Fig. 2 (A) Latent generative landscape (LGL) trained with sequences of the  $\alpha/\beta$  hydrolase (ABH) superfamily acting on halide bonds (GO:0016824), with mapped haloacetate dehalogenases (HAcD; GO:0018785; pink circles), haloalkane dehalogenases (HLD; GO:0018786; orange circles), and one sequence with hydrolase activity acting on halide bonds in C-halide compounds (GO:0019120; brown circle). (B) Known HAcDs (pink squares) and HLDs (orange squares), along with sequences of unknown function selected for testing (red triangles), mapped onto the LGL. The numbers in panels B and C correspond to the enzyme entries in Table 1. (C) Qualitative phenol red activity for the negative (–) and positive (+) control reactions without enzymes along with the select enzymes in panel B for each substrate. Activity is calculated by normalizing the average absorbance value at 560 nm to that of the negative control for the corresponding substrate. The normalized values and raw absorbance data with standard deviations are shown in Fig. S14.

(lower sequence energy) form dark blue basins corresponding to groups of sequences sharing similar evolutionary and functional characteristics, typically resulting in more stable and functional proteins. High Hamiltonian scores (higher sequence energy) create bright green barriers that separate distinct regions of sequence space, with sequences less likely to be stable and less explored by the extant dataset. This landscape representation enables the visualization and analysis of polygenetic relationships, functional diversity and evolutionary trajectories within protein family. For this work, the LGL framework was used to train a VAE on the MSA from above, and a Hamiltonian score assigned fitness as a statistical energy to each sequence in the landscape. The training sequences with their corresponding predicted molecular function annotation haloalkane dehalogenases (GO:0018785) or haloacetate dehalogenases (GO:0018786) are shown in the LGL map of the annotated training data (Fig. 2A), and the unannotated training sequences are mapped in the LGL map in Fig. S3.

### Plasmid design and preparation

The plasmids encoding the genes with the following UniProt accession numbers were synthesized by GenScript: A0A5P9PYN8, A0A5P9CV11, A0A960H4U9, A0A4V6IMR0, Q6NAM1, A0ABF7PGA4, A0A840N899, K8NY92, and A0A4Z0BVY8. Each gene was codon-optimized for expression in *Escherichia coli* and cloned between the NdeI and SalI restriction sites in the pET-28a(+) vector, resulting in an N-terminally polyhistidine-tagged enzyme. The nucleotide and amino acid sequences are shown in Fig. S4–S12.

Each plasmid was prepared by reconstituting a 4  $\mu\text{g}$  freeze-dried stock in 20  $\mu\text{L}$  of autoclaved water. A 1  $\mu\text{L}$  aliquot of this reconstituted plasmid was then diluted into 39  $\mu\text{L}$  of autoclaved water to achieve a final concentration of 5  $\text{ng } \mu\text{L}^{-1}$ .

Subsequently, 1  $\mu\text{L}$  of the diluted plasmid was transformed into *E. coli* 10 G ELITE Competent Cells (Lucigen) using an electroporator (MicroPulser, Bio-Rad Laboratories). The resulting transformation mixture was diluted with pre-warmed Super Optimal Broth with Catabolite Repression (SOC) media and incubated for 60 min at 37  $^{\circ}\text{C}$  with shaking at 225 rpm (Benchtop Shaking Incubator 6790, Corning). This mixture was then plated onto Miller's Luria Broth (LB) agar containing 50  $\mu\text{g mL}^{-1}$  kanamycin and incubated for 14 h at 37  $^{\circ}\text{C}$  (Model 12–140 Incubator, Quincy Lab). Individual colonies were selected and inoculated into 5 mL of LB media supplemented with 50  $\mu\text{g mL}^{-1}$  kanamycin, and then incubated for 16 h at 30  $^{\circ}\text{C}$  with shaking at 230 rpm (New Brunswick Innova 42R, Eppendorf). Finally, 2 mL of the culture was harvested *via* centrifugation at 8,000g (5424 R Centrifuge, Eppendorf) for 3 min at room temperature, and the plasmid was isolated using the QIAprep Spin Miniprep Kit (Qiagen).

### Protein expression and purification

Protein expression and purification were performed by adapting and modifying a previously established protocol, with specific expression conditions for each protein detailed in Table S3.<sup>68</sup> In general, the commercial plasmid was transformed into *E. coli* EXPRESS BL21 (DE3) (Lucigen) cells *via* electroporation, and the recovery and plating process followed the procedure described above. For expression, single colonies were inoculated into 10 mL of either LB or Terrific Broth (TB) containing 50  $\mu\text{g mL}^{-1}$  kanamycin and incubated at 30  $^{\circ}\text{C}$  for 14 h with shaking at 230 rpm. The following day, 2.5 mL of the overnight culture was diluted into 600 mL of LB or TB media (supplemented with 50  $\mu\text{g mL}^{-1}$  kanamycin) and incubated at 37  $^{\circ}\text{C}$  for 3 h with shaking at 250 rpm (New Brunswick Innova 44R, Eppendorf). Following this incubation period, the shaker was gradually cooled to 30  $^{\circ}\text{C}$  or 18  $^{\circ}\text{C}$  while shaking for 15–30 min. The



protein expression was induced by adding 300  $\mu\text{L}$  isopropyl  $\beta$ -D-1-thiogalactopyranoside (IPTG) from a 1 M stock solution or by relying on leaky expression, and the culture was incubated for an additional 21 h at 250 rpm. Finally, the culture was harvested by centrifugation at 3200g (5810 R Centrifuge, Eppendorf) for 30 min at 4  $^{\circ}\text{C}$ . The resulting cell pellet was resuspended in pre-chilled 20 mM Tris buffer at pH 7.5, 4  $^{\circ}\text{C}$  with 200 mM NaCl and stored at  $-20^{\circ}\text{C}$ .

Prior to purification, the cell pellet was thawed overnight at 4  $^{\circ}\text{C}$  and resuspended by vortexing. Cell lysis was carried out by sonication in an ice-water bath at 35% amplitude, with a 15 s pulse on and 45 s off pulse cycle for a total time of 5 min (Q500, QSonica). The resulting lysate was clarified *via* ultracentrifugation at 37 000g for 35 min at 4  $^{\circ}\text{C}$  (Optima XPN-80 Ultracentrifuge, Beckman Coulter). The clarified supernatant was loaded onto a pre-equilibrated 5 mL HisTrap Ni-NTA column (Cytiva Life Sciences) using a sample pump operating at 15  $^{\circ}\text{C}$  (NGC Chromatography System, Bio-Rad Laboratories). Following sample loading, the column was washed with 20 column volumes (CV) of running buffer (20 mM Tris buffer at pH 7.5, 15  $^{\circ}\text{C}$  with 200 mM NaCl and 30 mM imidazole). The polyhistidine-tagged protein was then eluted using a two-step method: first with 3 CV of 5% elution buffer (20 mM Tris buffer at pH 7.5, 15  $^{\circ}\text{C}$  with 200 mM NaCl and 500 mM imidazole) mixed with 95% running buffer, followed by a linear gradient of elution buffer from 5% to 100% over 20 CV. Affinity elution fractions with an absorbance signal at 280 nm were pooled and applied to a HiPrep 26/10 desalting column (Cytiva Life Sciences) equilibrated with 5 CV of 20 mM Tris buffer at pH 7.5, 15  $^{\circ}\text{C}$  with 150 mM NaCl. Desalted fractions exhibiting a 280 nm absorbance were subsequently pooled and concentrated using an Amicon Ultra-15 Centrifugal Filter Unit with a 10 kDa molecular weight cut-off (MWCO) (EMD Millipore). Finally, the concentrated enzyme sample was buffer exchanged twice (final dilution of 1:100) into a storage buffer of 20 mM Tris buffer at pH 7.5, 4  $^{\circ}\text{C}$  with 50 mM NaCl using a 10 kDa MWCO centrifugal filter. The final purified sample was stored at  $-20^{\circ}\text{C}$ . For each enzyme, two preparations were independently expressed and purified.

The purity of each enzyme preparation was evaluated using sodium dodecyl sulfate-polyacrylamide gel electrophoresis (SDS-PAGE) with methods from our previous study (Fig. S13).<sup>69</sup>

### Enzyme concentration determination

The concentration of each enzyme was determined using the theoretical molar extinction coefficient as described in our previous study.<sup>70</sup> The theoretical molar extinction coefficients for the full-length proteins with the polyhistidine tag of A0A5P9PYN8, A0A5P9CV11, A0A960H4U9, A0A4V6IMR0, Q6NAM1, A0ABF7PGA4, A0A840N899, K8NY92, and A0A4Z0BVY8 were determined to be 52 370  $\text{M}^{-1}\text{cm}^{-1}$ , 62 910  $\text{M}^{-1}\text{cm}^{-1}$ , 47 440  $\text{M}^{-1}\text{cm}^{-1}$ , 62 910  $\text{M}^{-1}\text{cm}^{-1}$ , 65 890  $\text{M}^{-1}\text{cm}^{-1}$ , 65 890  $\text{M}^{-1}\text{cm}^{-1}$ , 67 380  $\text{M}^{-1}\text{cm}^{-1}$ , 64 400  $\text{M}^{-1}\text{cm}^{-1}$ , and 58 900  $\text{M}^{-1}\text{cm}^{-1}$ , respectively, using the ProtParam tool in ExPASy.<sup>71</sup>

### Colorimetric pH assay for enzyme activity

A colorimetric pH assay with phenol red was used to qualitatively determine haloalkane and haloacetate dehalogenase activity by proton release for the following enzymes: A0A5P9PYN8, A0A5P9CV11, A0A960H4U9, A0A4V6IMR0, and Q6NAM1. All experimental methods and substrates were based on previously reported procedures.<sup>22,46,72</sup> For haloalkane dehalogenase activity, 1,2-dibromoethane, 4-bromobutyronitrile, and 1-iodopropane were tested, and for haloacetate dehalogenase activity, fluoroacetate, chloroacetate, and 2-fluoro-2-phenyl acetic acid were tested.<sup>43,46,73</sup> To prepare substrate stock solutions, haloalkane substrates were diluted to 200 mM in isopropyl alcohol (IPA), and haloacetate substrates were diluted to 287.7 mM in 25 mM MOPS at pH 7.5, 30  $^{\circ}\text{C}$ . These substrate stock solutions were combined with a 1  $\text{mg mL}^{-1}$  phenol red stock in water to make a substrate/phenol red reaction stock solution, resulting in a final reaction concentration of 20  $\mu\text{g mL}^{-1}$  phenol red, 10 mM substrate, 875  $\mu\text{M}$  MOPS buffer, and 5% IPA (for haloalkane reactions only). For haloalkane reaction stocks, the reaction stock contained 800  $\mu\text{L}$  of 1  $\text{mg mL}^{-1}$  phenol red, 2 mL of 200 mM substrate stock in IPA, and 1.4 mL of 25 mM MOPS at pH 7.5, 30  $^{\circ}\text{C}$ . For haloacetate reaction stocks, the reaction stock contained 800  $\mu\text{L}$  of 1  $\text{mg mL}^{-1}$  phenol red and 1.4 mL of 287.7 mM substrate stock. Enzyme stocks consisted of 4  $\mu\text{M}$  enzyme diluted in water from an 80  $\mu\text{M}$  enzyme stock in storage buffer (20 mM Tris buffer at pH 7.5, 4  $^{\circ}\text{C}$  with 50 mM NaCl), with the storage buffer being diluted 20-fold for the control reactions. Enzyme reactions contained a final concentration of 0.5  $\mu\text{M}$  enzyme and 125  $\mu\text{M}$  Tris buffer, while control reactions contained only 125  $\mu\text{M}$  Tris buffer. Each 1 mL reaction was carried out in a 1.5 mL microcentrifuge tube and contained: (i) 770  $\mu\text{L}$  of water for haloalkane reactions or 820  $\mu\text{L}$  of water for haloacetate reactions; and for positive control reactions, 20  $\mu\text{L}$  of water for haloalkane reactions or 70  $\mu\text{L}$  of water for haloacetate reactions; (ii) 105  $\mu\text{L}$  of the haloalkane phenol red stock or 55  $\mu\text{L}$  of the haloacetate phenol red stock; (iii) 125  $\mu\text{L}$  of the 4  $\mu\text{M}$  enzyme stock, or for control reactions, 125  $\mu\text{L}$  of 1 mM Tris buffer at pH 7.5, 4  $^{\circ}\text{C}$  with 2.5 mM NaCl; (iv) for the positive control, 750  $\mu\text{L}$  of 1 mM HCl was added for a final concentration of 750  $\mu\text{M}$  HCl. Reactions were carried out for two preparations per enzyme, with three reaction replicates per enzyme preparation and per substrate. Reactions proceed for 24 h at 30  $^{\circ}\text{C}$  (Thermo Scientific 2-Block Digital Dry Bath). Upon completion of the reaction, three 200  $\mu\text{L}$  aliquots from each reaction were transferred to a Greiner 96-well clear, PS, F-bottom microplate, and the absorbance at 560 nm (Tecan Spark Microplate Reader) was measured in triplicate and averaged for each reaction. Subsequently, the reaction replicates were then averaged for each enzyme preparation, and the values from the two enzyme preparations were finally averaged to obtain the reported raw absorbance, along with the propagated standard deviation. To calculate the relative activity for each reaction, the average absorbance was normalized to the negative control of the corresponding substrate. The values used to generate Fig. 2C are reported in Fig. S14.



## Identifying defluorinases from untrained, extant sequences with the LGL

To obtain a set of unannotated sequences with information excluded from the training data, we downloaded the entire ABH Pfam family (PF00561; 543 513 sequences) (Fig. S1). This was retrieved on August 12, 2025 using the InterPro API.<sup>74</sup> After removing training set sequences, the remaining 540 933 sequences were aligned using HMMER, which eliminated sequences with more than 5% contiguous gaps (12 consecutive gaps) and resulted in 296 598 sequences (Fig. S15).<sup>75</sup> Using the QuickGO API, sequences were annotated with their Gene Ontology (GO) predicted function, which was retrieved on August 13, 2025.<sup>66</sup> The resulting sequences were visualized on the LGL. All sequences in the haloacetate dehalogenase region were selected (3014 total sequences) and the frequency of their respective GO annotations were analyzed (Table S4). These sequences were further aligned *via* Clustal Omega with respect to Q6NAM1.<sup>76</sup> The residues corresponding to the Q6NAM1 active site were extracted and visualized with WebLogo.<sup>77,78</sup> Based on the three most frequently occurring GO annotations, sequences with conserved active site residues, less than three cysteines, and an isoelectric point (pI) less than 6.9 were selected for expression and characterization (Table S4). These included (i) A0A840N899 and K8NY92 (GO: 0016787; hydrolase activity), (ii) A0A4Z0BVY8 (GO:0047372; monoacylglycerol lipase activity), and (iii) A0ABF7PGA4 (no GO annotation). After being identified for initial evaluation, A0ABF7PGA4 was subsequently annotated with hydrolase activity by QuickGO (January 28, 2026). The MSA for these selected sequences was generated using Clustal Omega (Fig. S16).<sup>76</sup> A summary of pairwise identities pertaining to the training set annotated as haloacetate dehalogenases, the 3014 sequences selected from the haloacetate dehalogenase region, and the enzymes tested in this study are reported in Fig. S17 using the MSA for plotting onto the LGL (HMMER alignment with 5% (12) consecutive gaps removed).

## Enzyme unfolding temperature determination

To measure the ( $T_m$ ) of each enzyme, differential scanning fluorimetry (DSF) methods were adapted from our previous study.<sup>69</sup> In brief, the purified enzymes were adjusted to a concentration of 20  $\mu$ M using a buffer containing 20 mM Tris buffer at pH 7.5, 4  $^{\circ}$ C with 50 mM NaCl. Separately, a dye solution was prepared by diluting 3  $\mu$ L of 5000X SYPRO Orange Protein Gel Stain into 1.5 mL of the same buffer. To set up the assay, 15  $\mu$ L of the diluted enzyme and 15  $\mu$ L of the diluted SYPRO Orange solution were combined into the wells of a MicroAmp Fast Optical 96-Well reaction plate. This yielded a final assay mixture consisting of 10  $\mu$ M enzyme and 5X SYPRO Orange dye in 20 mM Tris buffer at pH 7.5, 4  $^{\circ}$ C with 50 mM NaCl. After sealing with a MicroAmp Optical Adhesive Film, the plate was centrifuged at 800g for 2 min at room temperature (5810 R Centrifuge, Eppendorf). Thermal shift assays were then performed on a QuantStudio 6 Flex Real-Time PCR System (Applied Biosystems). The instrument was configured to use ROX as the reporter dye, with both the quencher and passive

reference disabled. Measurements were recorded across a temperature range from 25  $^{\circ}$ C to 99  $^{\circ}$ C at a heating rate of 0.05  $^{\circ}$ C  $s^{-1}$  over 30 min. Post-run data analysis was conducted using Protein Thermal Shift Software v1.4. Raw fluorescence readings were normalized to facilitate sample comparison, and the  $T_m$  for each enzyme was calculated *via* the Boltzmann fit method. For each experiment, three technical replicates were averaged to determine the value for a single enzyme preparation, and the final  $T_m$  value is reported as the average of two enzyme preparations with the propagated standard deviation (Fig. S18).

## HPLC calibration curves

To quantify the enzyme activities, a calibration curve of the product (2-hydroxy-2-phenylacetic acid) and internal standard (IS, methyl benzoate) was generated (Fig. S19 and S20). Specifically, a stock solution of 100 mM 2-hydroxy-2-phenylacetic acid in 50 mM MOPS at pH 7, room temperature was first diluted to 30 mM in the same buffer, then serially diluted to 5, 10, 15, 20, and 25 mM. Next, 200  $\mu$ L of each diluted solution was transferred to a 1.5 mL microcentrifuge tube containing 300  $\mu$ L of 6.67 mM methyl benzoate in acetonitrile (HPLC grade). The product-IS solutions were mixed by vortexing and then clarified by centrifugation at 21 130g for 15 min at room temperature (5424 R Centrifuge, Eppendorf). After centrifugation, 450  $\mu$ L of the product-IS mixture for each standard was transferred to a 2 mL HPLC screw cap vial. The HPLC analysis was performed using a Shim-pack Velox C18 column (2.7  $\mu$ m, 3.0  $\times$  100 mm) with a Shim-pack Velox C18 EXP Guard Column Cartridge (2.7  $\mu$ m, 3.0  $\times$  5 mm) on a Shimadzu Prominence-i LC-2030C 3D system. The mobile phase A was water, adjusted to pH 2.7 with formic acid, and the mobile phase B was acetonitrile. A gradient of 5% to 95% mobile phase B was applied over 4 min, and then held at 95% mobile phase B for 3 min, using a flow rate of 0.4 mL  $min^{-1}$ . An absorbance wavelength of 254 nm was used to detect the product and internal standard. A background injection was performed using a mixture of 200  $\mu$ L water and 300  $\mu$ L acetonitrile. During data analysis, the background trace was subtracted from each sample trace using the Shimadzu Lab-Solutions software, and then all peaks were manually integrated. For each sample, three injections were conducted, and their average peak area constituted one technical replicate. Three technical replicates were analyzed per product concentration, and the final linear regression was constructed by plotting the ratio of the product peak area (PDT) to internal standard peak area (IS) (2-hydroxy-2-phenylacetate/methyl benzoate) on the y-axis with standard deviation *versus* the known product concentrations on the x-axis. The origin (0, 0) was included in the dataset, and the linear regression was forced through this point. This calibration curve reports the product concentration prior to the addition of IS.

## Optimization of enzyme reaction conditions

To optimize the reaction pH, reactions were performed in 50 mM sodium acetate buffer at pH 5, 50 mM MES buffer at pH 6, 50 mM MOPS buffer at pH 7, 50 mM bicine buffer at pH 8,



and 50 mM CHES buffer at pH 9 at 30 °C (Thermo Scientific 2-Block Digital Dry Bath). To remain within the calibration curve range due to its high reactivity, the A0A4Z0BVY8 reaction was limited to 10 min. All other enzyme reactions for pH optimization were carried out for 120 min. To prepare the substrate solutions, racemic 2-fluoro-2-phenylacetic acid was dissolved in each buffer at 25 mM. To account for temperature-dependent shifts, the pH of the substrate solution was adjusted and confirmed at each reaction temperature. Each enzyme was diluted to 20 μM using a buffer containing 20 mM Tris buffer at pH 7.5, 4 °C with 50 mM NaCl. All the following reactions were carried out with the same enzyme stock solution. In each reaction, 5 μL of the 20 μM diluted enzyme solution was added to 195 μL of the 25 mM substrate solution in each buffer in a 1.5 mL microcentrifuge tube, resulting in a final concentration of 0.5 μM enzyme and 24.375 mM substrate in a final reaction volume of 200 μL. A control reaction was carried out for each condition containing 195 μL of the substrate solution in each buffer with 5 μL buffer containing 20 mM Tris buffer at pH 7.5, 4 °C with 50 mM NaCl. All reactions were quenched with the addition of 300 μL of acetonitrile containing 6.67 mM methyl benzoate as the internal standard. The quenched reactions were vortexed and clarified by centrifugation at 21 130g for 15 min at room temperature (5424 R Centrifuge, Eppendorf). After centrifugation, 450 μL of each reaction mixture was transferred to a 2 mL HPLC screw cap vial. A background injection was performed using a mixture of 200 μL of water and 300 μL of acetonitrile. During data analysis, the background trace was subtracted from each sample trace using the Shimadzu Lab-Solutions software, and then all peaks were manually integrated. For each reaction, two injections were performed, and the average peak areas of these injections constituted one technical replicate. The product concentration was determined for each technical replicate using the calibration curve described above using the peak areas of the internal standard and product. Three technical replicates were conducted for each enzyme preparation at a given reaction condition with one technical control reaction for the same condition. To account for background hydrolysis, the calculated product concentration produced by the control reaction was subtracted from that of each enzyme reaction. The three technical replicates were averaged for each enzyme preparation.

The resulting averaged product concentration was then used to calculate the total turnover number (TTN) using the following equation:

$$\text{TTN} = \frac{[\text{Product}]}{[\text{Enzyme}]}$$

The final TTN is reported as the average of two independent enzyme preparations with the propagated standard deviation. The calculated product concentrations and resulting TTNs for the pH optimization are reported in Tables S5–S10, with the compiled data reported in Fig. S21.

To optimize the reaction temperature, reactions were performed in 50 mM bicine buffer at pH 8 for 10 min (Thermo Scientific 2-Block Digital Dry Bath). For A0A4V6IMR0, Q6NAM1,

and A0ABF7PGA4, reactions were performed at 70 °C, 80 °C, and 90 °C, for A0A4Z0BVY8, K8NY92, and A0A840N899 reactions were performed at 60 °C, 70 °C, and 80 °C. To prepare the substrate solution, racemic 2-fluoro-2-phenylacetic acid was dissolved in 50 mM bicine buffer at pH 8 at 25 mM. To account for temperature-dependent shifts, the pH of the substrate solution was adjusted and confirmed at each reaction temperature. To prepare the enzyme solutions, A0A4Z0BVY8 was diluted to 4 μM and Q6NAM1 was diluted to 8 μM from the 20 μM stock solutions using a buffer containing 20 mM Tris buffer at pH 7.5, 4 °C with 50 mM NaCl. For all other enzymes, the 20 μM stock solutions were used. In each reaction, a 5 μL diluted enzyme solution (4 μM for A0A4Z0BVY8, 8 μM for Q6NAM1, and 20 μM for the rest of the enzymes) was added to 195 μL of the substrate solution in each buffer in a 1.5 mL microcentrifuge tube, with a final concentration of 0.1 μM for A0A4Z0BVY8, 0.25 μM for Q6NAM1, and 0.5 μM for the rest of the enzymes and 24.375 mM substrate in a final reaction volume of 200 μL.

The reaction work-up and data analysis were processed as described above. The calculated product concentrations and resulting TTNs for the temperature optimization are reported in Tables S11–S16, with the compiled data shown in Fig. S22.

### Enzyme enantioselectivity determination

To determine the enantioselectivity of each enzyme, 10 μL of the 20 μM enzyme solution was added to 195 μL of a 125 mM substrate solution prepared in 100 mM bicine buffer at pH 8 for reactions at 60 °C in a 1.5 mL microcentrifuge tube, resulting in a final concentration of 1 μM enzyme and 118.75 mM racemic 2-fluoro-2-phenylacetic acid in 200 μL. A control reaction was prepared without enzyme with buffer and substrate only. The reaction times were 1 h for A0A4Z0BVY8, 4 h for Q6NAM1, A0ABF7PGA4, K8NY92, and 8 h for A0A4V6IMR0 and A0A840N899 (Thermo Scientific 2-Block Digital Dry Bath). The reaction time was 8 h for the no enzyme control. All reactions were quenched first with 20 μL of 12 M hydrochloric acid and then extracted with ethyl acetate three times (2 × 500 μL, 1 × 300 μL). The extracted organic layers were transferred to a 1.5 mL microcentrifuge tube, dried with anhydrous sodium sulfate, and then centrifuged at 21 130g for 1 min at room temperature (5424 R Centrifuge, Eppendorf). The clarified solution was transferred to a 20 mL glass vial, and the solvent was removed by a rotary evaporator (IKA RV 8 with IKA VC 10 vacuum controller, IKA VACSTAR digital vacuum pump, and IKA HB 10 heating bath). Next, 1 mL of HPLC grade methanol was added to the vial, and the solution was transferred to a 1.5 mL microcentrifuge tube and clarified for at 21 130g for 1 min at room temperature (5424 R Centrifuge, Eppendorf). The resulting clarified solution was transferred to a 2 mL HPLC screw cap vial for analysis.

The enantioselectivity of the enzyme reactions was determined by normal phase HPLC (Agilent 1260 Infinity II LC System) with a Lux Amylose-1 column (3 μm, 250 × 4.6 mm) at 23 °C. The compounds were eluted with 95:5 hexane/isopropanol and 0.5% trifluoroacetic acid with a flow rate of 1 mL per min. The injection volume was 5 μL for each sample



**Table 1** Bioinformatic annotations, melting temperature ( $T_m$ ), and catalytic performance of the enzymes tested on racemic 2-fluoro-2-phenylacetate (compound 3). Data are reported as the average with standard deviation of two independent enzyme preparations

Enzyme number	UniProt accession number	GO molecular function	$T_m$ (°C)	Reaction temperature (°C)	TTN <sup>a</sup>	4a ee <sup>b</sup> (%)	4b ee <sup>c</sup> (%)
1	A0A5P9PYN8	Haloalkane dehalogenase	67.85 ± 0.08	— <sup>d</sup>	—	—	—
2	A0A5P9CV11	Haloacetate dehalogenase	54.28 ± 0.07	—	—	—	—
3	A0A960H4U9	Haloalkane dehalogenase	50.40 ± 0.17	—	—	—	—
4	A0A4V6IMR0	Haloacetate dehalogenase	88.03 ± 0.26	70	5671 ± 128	87 ± 0	93 ± 0
5	Q6NAM1	Haloacetate dehalogenase	92.14 ± 0.15	90	22 176 ± 1102	91 ± 0	94 ± 0
6	A0ABF7PGA4	No annotation	90.74 ± 0.15	90	18 129 ± 485	91 ± 0	94 ± 0
7	A0A840N899	Hydrolase	78.85 ± 0.11	70	8911 ± 388	92 ± 1	93 ± 0
8	K8NY92	Hydrolase	81.42 ± 0.16	70	10 752 ± 837	89 ± 1	94 ± 0
9	A0A4Z0BVY8	Monoacylglycerol lipase	78.61 ± 0.11	60	59 828 ± 1241	99 ± 0	95 ± 0

<sup>a</sup> TTN, total turnover number. <sup>b</sup> Percent ee, enantiomeric excess, of compound 4a ((R)-2-fluoro-2-phenylacetate). <sup>c</sup> Percent ee of compound 4b ((R)-2-hydroxy-2-phenylacetate). <sup>d</sup> —, not determined.

and the absorbance wavelength was monitored at 210 nm. Commercial racemic 2-fluoro-2-phenylacetic acid, (R)-2-fluoro-2-phenylacetic acid, racemic 2-hydroxy-2-phenylacetic acid, (R)-2-hydroxy-2-phenylacetic acid, and (S)-2-hydroxy-2-phenylacetic acid were used as references. One control reaction and two enzyme reactions (one from each enzyme preparation) were evaluated, and all peaks were manually integrated. All parameters, including Retention Time (min), Area, Height, Width, Area%, and Symmetry, were analyzed with the Agilent ChemStation software (Tables S17–S24 and Fig. S23–S29). Enantiomeric excess (ee) was calculated for each compound and enzyme preparation by subtracting the Area % for the two enantiomers. The average ee with standard deviation for each enzyme is reported in Table 1 and Table S25.

### AI disclosure

Claude Sonnet 4.5 was used to support generation of the Python code for sequence extraction/annotation and data visualization.

## Results and discussion

The LGL framework learns sequence features from a multiple sequence alignment (MSA) of extant proteins (Fig. S1).<sup>58,75</sup> From the MSA, the VAE learns to encode sequences into a two-dimensional latent space, from which 250 000 grid points can then be decoded back into sequences.<sup>64</sup> In parallel, DCA of coevolved residues in the MSA is then used to infer a Potts Hamiltonian model that assigns a statistical energy (Hamiltonian) score to each sequence, visualized on a color scale in a third dimension (Fig. 2A).<sup>58,59</sup> Sequences that better satisfy the statistical constraints of the MSA are ranked with lower (favorable energy) Hamiltonian values and are located in dark blue regions of the map.<sup>58</sup> In contrast, sequences less explored by the extant dataset and more likely to be unstable have higher (unfavorable energy) Hamiltonian scores and fall in the bright green regions. Within the landscape, sequence location ultimately reflects phylogenetic and functional relationships, while Hamiltonian scores are an estimate of relative sequence fitness that delimit separable functional regions within the family.

To construct an LGL to discover fluoroacetate dehalogenases, we first trained the model on an aligned subset of 2753 sequences from the ABH superfamily annotated in Gene Ontology (GO) as hydrolases acting on acid halide bonds (GO:0016824) (Fig. S2 and S3).<sup>66,79</sup> Within this molecular function, two child terms define more specialized activities: diisopropyl-fluorophosphatase activity (GO:0047862) and hydrolase activity acting on acid halide bonds in C-halide compounds (GO:0019120). Because no sequences in the training set were annotated with GO:0047862, the functional space captured by the LGL reflects GO:0019120 and was dominated by the lower-level child terms associated with the ABH superfamily: haloacetate dehalogenase activity (GO:0018785) and haloalkane dehalogenase activity (GO:0018786) (Fig. S2). We used this curated dataset to characterize sequence variability with a degree of functional annotation.

Mapping the GO-annotated molecular functions of the training set onto the LGL revealed that sequences mostly clustered into distinct regions, with high Hamiltonian score barriers separating the two activities (Fig. 2A). To confirm this organization, we compiled and mapped experimentally validated haloalkane and haloacetate dehalogenases from the literature (Fig. 2B and Tables S1–S2). The locations of these sequences agreed with the respective GO-annotated regions, with only a few exceptions at the origin of the LGL, which typically exhibit unfavorable or higher Hamiltonian scores, containing sequences less represented by the training MSA.

Next, we sought to experimentally assess the functional organization of the LGL. We used the LGL as a guide to choose enzymes from various parts of the cluster. Based on regions with specific GO molecular function annotations, we selected A0A5P9PYN8 (haloalkane dehalogenase; enzyme 1) and A0A5P9CV11 (haloacetate dehalogenase; enzyme 2) from regions lacking previously validated enzymes; A0A960H4U9 (haloalkane dehalogenase; enzyme 3) and A0A4V6IMR0 (haloacetate dehalogenase; enzyme 4) from regions containing previously validated enzymes (Fig. 2B, S4–S7 and Table 1). Q6NAM1 (enzyme 5) was included as a positive control for comparison in all assays (Fig. 2B and S8). All enzymes were



expressed in *Escherichia coli* with an N-terminal polyhistidine tag and purified by nickel-affinity chromatography (Table S3 and Fig. S13). Enzymatic activity toward representative haloalkane substrates (4-bromobutyronitrile, 1-iodopropane, and 1,2-dibromoethane) and haloacetate substrates (chloroacetate, fluoroacetate, and 2-fluoro-2-phenylacetate) was evaluated using a colorimetric pH-shift assay with phenol red to detect proton release upon hydrolysis (Fig. 2C and S14).<sup>22,43,46,72,73</sup> Notably, A0A960H4U9 and A0A4V6IMR0 displayed activity toward their predicted substrate classes, whereas A0A5P9PYN8 and A0A5P9CV11 showed no measurable activity, suggesting either that the assay conditions were not optimal or that the actual functions may differ from the currently assigned annotations.

Finally, we asked whether the functional organization of the LGL could be applied more broadly to reannotate extant sequences with incorrect or ambiguous GO-term assignments. To do this, we collated and curated the 543 513 sequences from the ABH superfamily (InterPro; August 12, 2025, Fig. S1).<sup>74,80</sup> After removing training-set sequences (GO:0016824) and those containing more than 5% contiguous gaps, a total of 296 598 sequences were mapped onto the LGL (Fig. S15). Interestingly, 3014 sequences were in the haloacetate dehalogenase region (Fig. 3A). Furthermore, multiple sequence alignment indicated that residues needed for fluoroacetate recognition and catalysis

in Q6NAM1 are conserved across this subset of sequences, suggesting potential defluorinase activity (Fig. 3B).<sup>76–78</sup>

To investigate whether these sequences indeed encode defluorinases, we selected representative sequences for experimental characterization belonging to the three most frequently occurring GO annotations: hydrolase activity, monoacylglycerol lipase activity, and no annotation (Table S4). We hypothesized that we could increase the likelihood of identifying active enzymes by focusing on sequences located near A0A4V6IMR0 and Q6NAM1 (Fig. 3A), while also considering biochemical properties relevant to expression and purification (*i.e.*, cysteine content, isoelectric point). The selected candidates were A0ABF7PGA4, A0A840N899, K8NY92, and A0A4Z0BVY8 (enzymes 6–9, respectively) (Table 1 and Fig. S9–S12, S16, S17). After expressing and purifying these candidates as described above, we measured the unfolding temperature ( $T_m$ ) of all enzymes to determine enzyme stability and establish optimal reaction conditions for further testing of the putative defluorinases (Fig. S13, S18 and Table S3).<sup>81</sup> Q6NAM1, in line with prior data, and its close homolog A0ABF7PGA4 (98% identity) exhibited exceptionally high  $T_m$  values ( $>90$  °C).<sup>43</sup> Despite sharing modest sequence identity with Q6NAM1 (49–79%), A0A4V6IMR0, A0A840N899, K8NY92, and A0A4Z0BVY8 were also thermostable ( $T_m > 70$  °C) (Table 1 and Fig. S17).<sup>43,76</sup>

Lastly, we quantified the defluorination activity of these enzymes together with Q6NAM1 and A0A4V6IMR0 using 2-fluoro-2-phenylacetate (compound 3) as the substrate (Fig. 1C and Table 1). Reaction conditions were screened across pH and temperature and analyzed by reverse-phase high-performance liquid chromatography (HPLC) (Fig. S19–S22 and Tables S5–S16). All enzymes shared the same pH optimum at pH 8, but their optimal reaction temperatures ranged from 60 °C to 90 °C, consistent with their measured unfolding temperatures (Table 1). Overall, the total turnover numbers (TTNs) ranged from 5671 to 59 828 in 10 min (Table 1 and Fig. S22). Notably, A0A4Z0BVY8 exhibited approximately 2.7-fold greater activity than Q6NAM1, the current state-of-the-art enzyme. Each enzyme maintained a preference for the (S)-enantiomer substrate, generating the (R)-enantiomer product with high enantioselectivity ( $>93\%$ ) (Tables 1, S17–S24 and Fig. S23–S29).<sup>37,43</sup> This conserved stereochemical outcome is in line with the  $S_N2$  mechanism known for Q6NAM1.<sup>14,35,39</sup>

## Conclusions

Motivated by the chemical significance and biotechnological potential of enzymatic carbon–fluorine bond cleavage, we applied our machine learning-based LGL framework to uncover hydrolytic defluorinases within the ABH superfamily. By training this model on GO-annotated hydrolases acting on acid halide bonds, the LGL revealed that distinct regions of latent space could be associated with particular enzyme functions. Specific examples from the literature, together with our experimental validation, confirmed the accuracy of the LGL designations for haloalkane and haloacetate dehalogenases, highlighting the potential to reannotate extant sequences with incorrect or ambiguous GO-term assignments. In this pursuit,

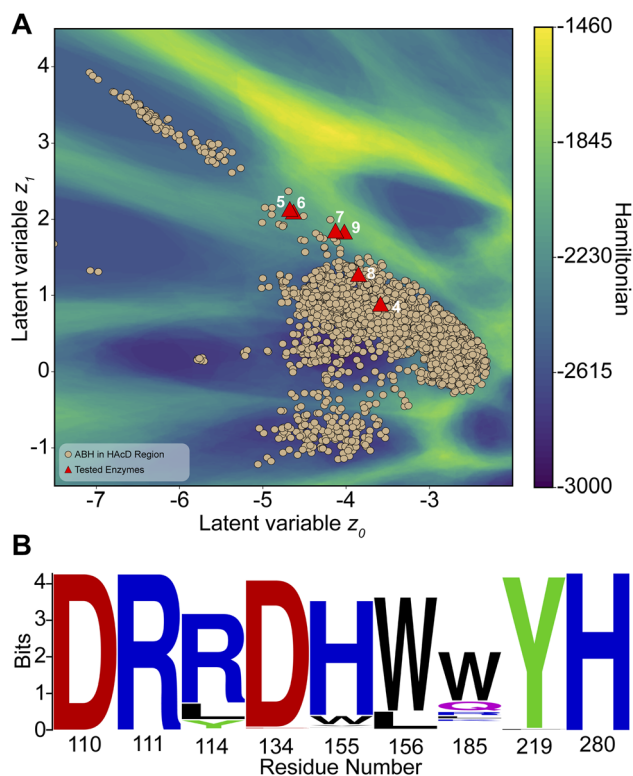


Fig. 3 (A) ABH sequences outside of the training set (tan circles) mapped within the HAcD region of the LGL. Sequences selected for testing are indicated with numbered red triangles that correspond to the enzyme entries in Table 1. (B) WebLogo analysis of the active site residues in Q6NAM1 for the ABH sequences in the HAcD region shown in panel A.



we identified a total of 3014 putative haloacetate dehalogenases and discovered five new fluoroacetate dehalogenases with a range of defluorination activities. A notable example is A0A4Z0BVY8 that surpassed the activity of the current state-of-the-art enzyme Q6NAM1 on 2-fluoro-2-phenylacetic acid.

Our results establish that the LGL framework can resolve functionally distinct carbon–halogen bond chemistries within the ABH sequence space, highlighting how LGLs can help reveal enzymes that are not readily accessible through traditional similarity-based annotations. While the annotated training sequences and the identified defluorinases cluster within a confined region of the LGL, they originate from diverse microbial species and span a wide range of sequence identities ruling out traditional phylogenetic relationships (Fig. S17 and Table S25). Moreover, the experimentally characterized defluorinases share identical active site residues, yet exhibit markedly different catalytic efficiencies. We conclude that although LGL regions delimited by latent coordinates are predictive of similar functionalities, their Hamiltonian scores are insufficient to predict specific values of catalytic activities (Table S25). Instead, global sequence context and structural dynamics are likely critical factors for function and will be important directions for future mechanistic investigations. Finally, the presence of thousands of putative defluorinases, despite the rarity of fluorinated natural products, suggests that this chemistry may be more deeply embedded in the ABH sequence space than previously recognized. This raises questions regarding the natural roles of these enzymes and the evolutionary pressures that shaped them. To close, our approach lays the foundation for unraveling how natural and engineered protein sequence space encodes for rare and challenging carbon–fluorine bond chemistry in the ABH superfamily and beyond, opening new opportunities to advance defluorinases for sustainable synthesis and bioremediation applications.

## Author contributions

K. J.: data curation, formal analysis, investigation, methodology, validation, visualization, writing – original draft, writing – review & editing. S. S. B.: data curation, formal analysis, investigation, methodology, validation, visualization, writing – original draft, writing – review & editing. C. Z.: formal analysis, investigation, methodology, software, validation, visualization. M. N.: formal analysis, investigation, methodology, software, validation, visualization, writing – review & editing. J. A. D. L. P.: formal analysis, investigation, methodology, software, validation, visualization, writing – review & editing. E. K. P.: formal analysis, investigation, writing – review & editing. N. K.: methodology. F. M.: conceptualization, funding acquisition, supervision, writing – review & editing. S. C. D.: conceptualization, funding acquisition, supervision, writing – review & editing.

## Conflicts of interest

A provisional patent application has been filed on behalf of K. J., S. S. B., C. Z., F. M., and S. C. D. The remaining authors have no conflicts of interest.

## Data availability

The data that support the findings of this study are available in the main text and supplementary information (SI). Sequence FASTA files and associated LGL files are available in a Zenodo repository (DOI: <https://doi.org/10.5281/zenodo.15485612>). The corresponding authors can be contacted for additional requests. Supplementary information is available. See DOI: <https://doi.org/10.1039/d6sc02671k>.

## Acknowledgements

Research support was provided to S.C.D. by the UT Dallas Sustainability Seed Program for Interdisciplinary Research and the Welch Foundation grant AT-2060-20240404; F.M. by the NIH grant R35GM133631 and the NSF CAREER Award MCB-1943442. The authors acknowledge the UTD Center for High-Throughput Reaction Discovery and Synthesis for assistance with chiral chromatography analysis; Genome Center at UT Dallas for access to qPCR instrumentation; the Office of Information Technology Cyberinfrastructure Research Computing (CIRC) at UT Dallas for providing for providing HPC and storage. This study does not represent the views of the supporting agencies and is the responsibility of the authors.

## References

- 1 R. Fuge, *Environ. Geochem. Health*, 1988, **10**, 51–61.
- 2 K. T. Koga and E. F. Rose-Koga, *C. R. Chim.*, 2018, **21**, 749–756.
- 3 W. H. Schlesinger, E. M. Klein and A. Vengosh, *Global Biogeochem. Cycles*, 2020, **34**, e2020GB006722.
- 4 J. J. Petkowski, S. Seager and W. Bains, *Sci. Rep.*, 2024, **14**, 15575.
- 5 B. D. Key, R. D. Howell and C. S. Criddle, *Environ. Sci. Technol.*, 1997, **31**, 2445–2454.
- 6 D. B. Harper, D. O'Hagan and C. D. Murphy, in *Natural Production of Organohalogen Compounds*, ed. G. Gribble, Springer Berlin Heidelberg, Berlin, Heidelberg, 2003, pp. 141–169.
- 7 C. Walsh, in *Advances in Enzymology and Related Areas of Molecular Biology*, ed. A. Meister, John Wiley & Sons, Inc., Hoboken, New Jersey, 1983, pp. 197–289.
- 8 D. S. Flournoy and P. A. Frey, *Biochemistry*, 1986, **25**, 6036–6043.
- 9 S. Li and L. P. Wackett, *Biochemistry*, 1993, **32**, 9355–9361.
- 10 D. J. T. Porter, J. A. Harrington, M. R. Almond, W. G. Chestnut, G. Tanoury and T. Spector, *Biochem. Pharmacol.*, 1995, **50**, 1475–1484.
- 11 I. P. Solyanikova, O. V. Moiseeva, S. Boeren, M. G. Boersma, M. P. Kolomytseva, J. Vervoort, I. M. C. M. Rietjens, L. A. Golovleva and W. J. H. van Berkel, *Appl. Environ. Microbiol.*, 2003, **69**, 5636–5642.
- 12 F. Bellezza, A. Cipiciani, G. Ricci and R. Ruzziconi, *Tetrahedron*, 2005, **61**, 8005–8012.
- 13 L. Williams, T. Nguyen, Y. Li, T. N. Porter and F. M. Raushel, *Biochemistry*, 2006, **45**, 7453–7462.



- 14 P. W. Y. Chan, A. F. Yakunin, E. A. Edwards and E. F. Pai, *J. Am. Chem. Soc.*, 2011, **133**, 7461–7468.
- 15 D. O'Hagan and H. Deng, *Chem. Rev.*, 2015, **115**, 634–649.
- 16 V. Agarwal, Z. D. Miles, J. M. Winter, A. S. Eustáquio, A. A. El Gamal and B. S. Moore, *Chem. Rev.*, 2017, **117**, 5619–5674.
- 17 Y. Wang and A. Liu, *Chem. Soc. Rev.*, 2020, **49**, 4906–4925.
- 18 L. Wu and H. Deng, *Org. Biomol. Chem.*, 2020, **18**, 6236–6240.
- 19 M. García-Ramos, A. Cuetos, W. Kroutil, G. Grogan and I. Lavandera, *ChemCatChem*, 2021, **13**, 3967–3972.
- 20 P. W. Y. Chan, N. Chakrabarti, C. Ing, O. Halgas, T. K. W. To, M. Wälti, A. Petit, C. Tran, A. Savchenko, A. F. Yakunin, E. A. Edwards, R. Pomès and E. F. Pai, *ChemBioChem*, 2022, **23**, e202100414.
- 21 Q. Huang, X. Zhang, Q. Chen, S. Tian, W. Tong, W. Zhang, Y. Chen, M. Ma, B. Chen, B. Wang and J. Wang, *ACS Catal.*, 2022, **12**, 265–272.
- 22 A. N. Khusnutdinova, K. A. Batyrova, G. Brown, T. Fedorchuk, Y. S. Chai, T. Skarina, R. Flick, A. Petit, A. Savchenko, P. Stogios and A. F. Yakunin, *FEBS J.*, 2023, **290**, 4966–4983.
- 23 M. F. Khan, S. Chowdhary, B. Kokschi and C. D. Murphy, *Environ. Sci. Technol.*, 2023, **57**, 9762–9772.
- 24 Y. Yu, F. Xu, W. Zhao, C. Thoma, S. Che, J. E. Richman, B. Jin, Y. Zhu, Y. Xing, L. Wackett and Y. Men, *Sci. Adv.*, 2024, **10**, eado2957.
- 25 L. P. Wackett and S. L. Robinson, *Biochem. J.*, 2024, **481**, 1757–1770.
- 26 C. M. Smorada, M. W. Sima and P. R. Jaffé, *Curr. Opin. Biotechnol.*, 2024, **88**, 103170.
- 27 L. Hendricks, C. R. Reinhardt, T. Green, L. Kunczynski, A. J. Roberts, N. Miller, N. Rafalin, H. J. Kulik, J. T. Groves and R. N. Austin, *J. Am. Chem. Soc.*, 2025, **147**, 9085–9090.
- 28 K. M. Cunningham, W. Shin and Z. J. Yang, *ChemPhysChem*, 2025, **26**, e202401130.
- 29 Y. Zhang, Y. Cao, C. V. Sastri and S. P. de Visser, *ACS Catal.*, 2025, **15**, 3898–3912.
- 30 X. Chen, Y. Zhang, J. Fu, Z. Chen, X. Zhou and X. Chu, *Commun. Chem.*, 2025, **8**, 396.
- 31 P. Goldman, *J. Biol. Chem.*, 1965, **240**, 3434–3438.
- 32 D. L. Ollis, E. Cheah, M. Cygler, B. Dijkstra, F. Frolow, S. M. Franken, M. Harel, S. J. Remington, I. Silman, J. Schrag, J. L. Sussman, K. H. G. Verschuere and A. Goldman, *Protein Eng. Des. Sel.*, 1992, **5**, 197–211.
- 33 M. Holmquist, *Curr. Protein Pept. Sci.*, 2000, **1**, 209–235.
- 34 K. Jitsumori, R. Omi, T. Kurihara, A. Kurata, H. Mihara, I. Miyahara, K. Hirotsu and N. Esaki, *J. Bacteriol.*, 2009, **191**, 2630–2637.
- 35 S. Miranda-Rojas and A. Toro-Labbé, *J. Chem. Phys.*, 2015, **142**, 194301.
- 36 T. Nakayama, T. Kamachi, K. Jitsumori, R. Omi, K. Hirotsu, N. Esaki, T. Kurihara and K. Yoshizawa, *Chem. Eur. J.*, 2012, **18**, 8392–8402.
- 37 J. Wang, A. Ilie, S. Yuan and M. T. Reetz, *J. Am. Chem. Soc.*, 2017, **139**, 11241–11247.
- 38 P. Mehrabi, E. C. Schulz, R. Dsouza, H. M. Müller-Werkmeister, F. Tellkamp, R. J. D. Miller and E. F. Pai, *Science*, 2019, **365**, 1167–1170.
- 39 Y. Yue, J. Fan, G. Xin, Q. Huang, J. Wang, Y. Li, Q. Zhang and W. Wang, *Environ. Sci. Technol.*, 2021, **55**, 9817–9825.
- 40 A. Bateman, M.-J. Martin, S. Orchard, M. Magrane, A. Adesina, S. Ahmad, E. H. Bowler-Barnett, H. Bye-A-Jee, D. Carpentier, P. Denny, J. Fan, P. Garmiri, L. J. da C. Gonzales, A. Hussein, A. Ignatchenko, G. Insana, R. Ishtiaq, V. Joshi, D. Jyothi, S. Kandasamy, A. Lock, A. Luciani, J. Luo, Y. Lussi, J. S. M. Marin, P. Raposo, D. L. Rice, R. Santos, E. Speretta, J. Stephenson, P. Tootoo, N. Tyagi, N. Urakova, P. Vasudev, K. Warner, S. Wijerathne, C. W.-H. Yu, R. Zaru, A. J. Bridge, L. Aimo, G. Argoud-Puy, A. H. Auchincloss, K. B. Axelsen, P. Bansal, D. Baratin, T. M. Batista Neto, M.-C. Blatter, J. T. Bolleman, E. Boutet, L. Breuza, B. C. Gil, C. Casals-Casas, K. C. Echioukh, E. Coudert, B. Cucho, E. de Castro, A. Estreicher, M. L. Famiglietti, M. Feuermann, E. Gasteiger, P. Gaudet, S. Gehant, V. Gerritsen, A. Gos, N. Gruaz, C. Hulo, N. Hyka-Nouspikel, F. Jungo, A. Kerhornou, P. Le Mercier, D. Lieberherr, P. Masson, A. Morgat, S. Paesano, I. Pedruzzi, S. Pilbout, L. Pourcel, S. Poux, M. Pozzato, M. Pruess, N. Redaschi, C. Rivoire, C. J. A. Sigrist, K. Sonesson, S. Sundaram, A. Sveshnikova, C. H. Wu, C. N. Arighi, C. Chen, Y. Chen, H. Huang, K. Laiho, M. Lehvaslaiho, P. McGarvey, D. A. Natale, K. Ross, C. R. Vinayaka, Y. Wang and J. Zhang, *Nucleic Acids Res.*, 2025, **53**, D609–D617.
- 41 J.-Q. Liu, T. Kurihara, S. Ichiyama, M. Miyagi, S. Tsunasawa, H. Kawasaki, K. Soda and N. Esaki, *J. Biol. Chem.*, 1998, **273**, 30897–30902.
- 42 S. Wang, Z. Cheng, Y. Xu, L. Yang, J.-B. Wang, Z. Tian and X. Qu, *Green Synth. Catal.*, 2020, **1**, 60–65.
- 43 H. Zhang, S. Tian, Y. Yue, M. Li, W. Tong, G. Xu, B. Chen, M. Ma, Y. Li and J. Wang, *ACS Catal.*, 2020, **10**, 3143–3151.
- 44 M. Hu and C. Scott, *Appl. Environ. Microbiol.*, 2024, **90**, e00157–24.
- 45 S. C. Jansen, P. van Beers and C. Mayer, *Angew. Chem., Int. Ed.*, 2026, **65**, e24234.
- 46 W. Y. Chan, M. Wong, J. Guthrie, A. V. Savchenko, A. F. Yakunin, E. F. Pai and E. A. Edwards, *Microb. Biotechnol.*, 2010, **3**, 107–120.
- 47 S. Farajollahi, N. V. Lombardo, M. D. Crenshaw, H.-B. Guo, M. E. Doherty, T. R. Davison, J. J. Steel, E. A. Almand, V. A. Varaljay, C. Sui-Hung, P. A. Mirau, R. J. Berry, N. Kelley-Loughnane and P. B. Dennis, *ACS Omega*, 2024, **9**, 28546–28555.
- 48 C. Badel, E. Bocconetti, R. Khodr, C. Husser, M. Ryckelynck and S. Vuilleumier, *Microbiol. Resour. Announc.*, 2025, **14**, e00812–e00824.
- 49 S. I. Probst, F. D. Felder, V. Poltorak, R. Mewalal, I. K. Blaby and S. L. Robinson, *Proc. Natl. Acad. Sci. U.S.A.*, 2025, **122**, e2504122122.
- 50 A. Forouzandeh, M. S. L. Schlosser, A. N. Vernon and T. K. Nielsen, *bioRxiv*, 2025, preprint, DOI: [10.1101/2025.07.23.666183](https://doi.org/10.1101/2025.07.23.666183).
- 51 A. Bairoch, *Nucleic Acids Res.*, 2000, **28**, 45–48.
- 52 F. Ozhelvaci and K. Steczkiewicz, *Proteins: Struct., Funct., Bioinf.*, 2025, **93**, 855–870.



- 53 T. Yu, H. Cui, J. C. Li, Y. Luo, G. Jiang and H. Zhao, *Science*, 2023, **379**, 1358–1363.
- 54 P. Kohout, M. Vasina, M. Majerova, V. Novakova, J. Damborsky, D. Bednar, M. Marek, Z. Prokop and S. Mazurenko, *JACS Au*, 2025, **5**, 838–850.
- 55 B. Norton-Baker, E. Komp, J. E. Gado, M. C. R. Denton, I. I. Mathews, N. P. Murphy, E. Erickson, O. O. Storment, R. Sarangi, N. P. Gauthier, J. E. McGeehan and G. T. Beckham, *ACS Catal.*, 2025, **15**, 16070–16083.
- 56 T. Lambert, A. Tavakoli, G. Dharuman, J. Yang, V. Bhethanabotla, S. Kaur, M. Hill, A. Ramanathan, A. Anandkumar and F. H. Arnold, *Nat. Commun.*, 2026, **17**, 1680.
- 57 F. Moorhoff, Y. Zhang, S. Qiu, W. Dong, D. Medina-Ortiz, J. Zhao and M. D. Davari, *ACS Catal.*, 2026, **16**, 12–30.
- 58 C. Ziegler, J. Martin, C. Sinner and F. Morcos, *Nat. Commun.*, 2023, **14**, 2222.
- 59 F. Morcos, A. Pagnani, B. Lunt, A. Bertolino, D. S. Marks, C. Sander, R. Zecchina, J. N. Onuchic, T. Hwa and M. Weigt, *Proc. Natl. Acad. Sci. U.S.A.*, 2011, **108**, E1293–E1301.
- 60 A. J. Riesselman, J. B. Ingraham and D. S. Marks, *Nat. Methods*, 2018, **15**, 816–822.
- 61 P. K. Diederik and W. Max, arXiv, 2019, preprint, arXiv:1906.02691, DOI: [10.48550/arXiv.1906.02691](https://doi.org/10.48550/arXiv.1906.02691).
- 62 X. Ding, Z. Zou and C. L. Brooks III, *Nat. Commun.*, 2019, **10**, 5644.
- 63 F. Montalvillo Ortega, F. Hossain, V. V. Volobouev, G. Meloni, H. Torabifard and F. Morcos, *ACS Cent. Sci.*, 2025, **11**, 1452–1466.
- 64 D. Shukla, J. Martin, F. Morcos and D. A. Potoyan, *J. Chem. Theory Comput.*, 2025, **21**, 3277–3287.
- 65 J. Mistry, S. Chuguransky, L. Williams, M. Qureshi, G. A. Salazar, E. L. L. Sonhammer, S. C. E. Tosatto, L. Paladin, S. Raj, L. J. Richardson, R. D. Finn and A. Bateman, *Nucleic Acids Res.*, 2021, **49**, D412–D419.
- 66 D. Binns, E. Dimmer, R. Huntley, D. Barrell, C. O'Donovan and R. Apweiler, *Bioinformatics*, 2009, **25**, 3045–3046.
- 67 R. P. Huntley, T. Sawford, M. J. Martin and C. O'Donovan, *Gigascience*, 2014, **3**, 4.
- 68 K. Ji, E. K. Pack, C. Maydew, K. A. Alberto, S. Abeyrathna, R. L. E. Villones, H. Gull, G. Meloni, S. O. Nielsen and S. C. Dodani, *Commun. Chem.*, 2025, **8**, 275.
- 69 K. Ji, K. Baek, W. Peng, K. A. Alberto, H. Torabifard, S. O. Nielsen and S. C. Dodani, *Chem. Commun.*, 2022, **58**, 965–968.
- 70 W. S. Y. Ong, K. Ji, V. Pathiranage, C. Maydew, K. Baek, R. L. E. Villones, G. Meloni, A. R. Walker and S. C. Dodani, *Angew. Chem., Int. Ed.*, 2023, **62**, e202302304.
- 71 E. Gasteiger, A. Gattiker, C. Hoogland, I. Ivanyi, R. D. Appel and A. Bairoch, *Nucleic Acids Res.*, 2003, **31**, 3784–3788.
- 72 P. Holloway, J. T. Trevors and H. Lee, *J. Microbiol. Methods*, 1998, **32**, 31–36.
- 73 T. Koudelakova, E. Chovancova, J. Brezovsky, M. Monincova, A. Fortova, J. Jarkovsky and J. Damborsky, *Biochem. J.*, 2011, **435**, 345–354.
- 74 M. Blum, A. Andreeva, L. C. Florentino, S. R. Chuguransky, T. Grego, E. Hobbs, B. L. Pinto, A. Orr, T. Paysan-Lafosse, I. Ponamareva, G. A. Salazar, N. Bordin, P. Bork, A. Bridge, L. Colwell, J. Gough, D. H. Haft, I. Letunic, F. Llinares-López, A. Marchler-Bauer, L. Meng-Papaxanthos, H. Mi, D. A. Natale, C. A. Orengo, A. P. Pandurangan, D. Piovesan, C. Rivoire, C. J. A. Sigris, N. Thanki, F. Thibaud-Nissen, P. D. Thomas, S. C. E. Tosatto, C. H. Wu and A. Bateman, *Nucleic Acids Res.*, 2025, **53**, D444–D456.
- 75 S. C. Potter, A. Luciani, S. R. Eddy, Y. Park, R. Lopez and R. D. Finn, *Nucleic Acids Res.*, 2018, **46**, W200–W204.
- 76 F. Madeira, N. Madhusoodanan, J. Lee, A. Eusebi, A. Niewielska, A. R. N. Tivey, R. Lopez and S. Butcher, *Nucleic Acids Res.*, 2024, **52**, W521–W525.
- 77 T. D. Schneider and R. M. Stephens, *Nucleic Acids Res.*, 1990, **18**, 6097–6100.
- 78 G. E. Crooks, G. Hon, J.-M. Chandonia and S. E. Brenner, *Genome Res.*, 2004, **14**, 1188–1190.
- 79 R. P. Huntley, T. Sawford, P. Mutowo-Meullenet, A. Shypitsyna, C. Bonilla, M. J. Martin and C. O'Donovan, *Nucleic Acids Res.*, 2015, **43**, D1057–D1063.
- 80 T. Paysan-Lafosse, A. Andreeva, M. Blum, S. R. Chuguransky, T. Grego, B. L. Pinto, G. A. Salazar, M. L. Bileschi, F. Llinares-López, L. Meng-Papaxanthos, L. J. Colwell, N. V. Grishin, R. D. Schaeffer, D. Clementel, S. C. E. Tosatto, E. Sonhammer, V. Wood and A. Bateman, *Nucleic Acids Res.*, 2025, **53**, D523–D534.
- 81 F. H. Niesen, H. Berglund and M. Vedadi, *Nat. Protoc.*, 2007, **2**, 2212–2221.

